RAA 2021 Vol. **21** No. **6**, 135(8pp) doi: 10.1088/1674-4527/21/6/135

http://www.raa-journal.org *http://iopscience.iop.org/raa*

Research in Astronomy and Astrophysics

Obtaining space-based SDO/AIA solar UV and EUV images from ground-based Hα observations by deep learning

Tie Liu (刘铁)[1,2], Ying-Na Su (宿英娜)[1,2], Li-Ming Xu (徐黎明)[3] and Hai-Sheng Ji (季海生)[1,2]

[1] Key Laboratory of Dark Matter and Space Astronomy, Purple Mountain Observatory, Chinese Academy of Sciences, Nanjing 210023, China; *liutie@pmo.ac.cn; ynsu@pmo.ac.cn*

[2] School of Astronomy and Space Science, University of Science and Technology of China, Hefei 230026, China

[3] Jiangsu Urban and Rural Construction College, Changzhou 213147, China

Received 2020 November 6; accepted 2021 January 3

Abstract In this work, we explore the mappings from solar images taken in Hα (6563 Å) by the Global Oscillation Network Group (GONG) on the ground to those observed in eight different wavelengths (94, 131, 171, 193, 211, 304, 335 and 1600 Å) by SDO/AIA in space. Eight mappings are built by training the conditional Generative Adversarial Networks (cGANs) on datasets with 500 paired images, which are [Hα, AIA94], [Hα, AIA131], [Hα, AIA171], [Hα, AIA193], [Hα, AIA211], [Hα, AIA304], [Hα, AIA335] and [Hα, AIA1600]. We evaluate the eight trained cGANs models on validation and test datasets with 154-pair images and 327-pair images, respectively. The model generated fake AIA images match the corresponding observed AIA images well on large-scale structures such as large active regions and prominences. But the small-scale flare loops and filament threads are difficult to reconstruct. Four quantitative comparisons are carried out on the validation and test datasets to score the mappings. We find that the model-generated images in 304 and 1600 Å match the corresponding observed images best. This exploration suggests that the cGANs are promising methods for mappings between ground-based Hα and space-based EUV/UV images, while some improvements are necessary.

Key words: methods: analytical — techniques: image processing — Sun: corona — Sun: UV radiation

1 INTRODUCTION

Astronomical observations have entered the multi-messenger era over the past few decades. Ground-based and space-based telescopes and equipment have been built to obtain information of the universe from radio to X-ray. In the case of solar observations, images of the Sun are obtained through not only ground-based telescopes (e.g., New Vacuum Solar Telescope (NVST; Liu et al. 2014) and Goode Solar Telescope (GST; Cao et al. 2010)) but also space missions such as Hinode (Kosugi et al. 2007) and Solar Dynamics Observatory (SDO; Pesnell et al. 2012). Multiple imaging devices are observing the Sun nearly simultaneously and almost from the same angle. In addition to small-scale structures, we have to pay more attention to large solar activities, because some of them may lead to catastrophic space weather and damage the safety of satellites and astronauts. There is a serious problem in astronomical spectroscopy, which is the absorption of light in the Earth's atmosphere. Usually, ground-based equipment can only collect information at radio and visible light passbands. While ultraviolet (UV), extreme ultraviolet (EUV) and X-ray passbands are only available in the outer space. On the one hand, launching satellites with observation equipment is more expensive and technically difficult than building ground-based equipment. On the other hand, observations in UV and EUV passbands can monitor and predict solar flares and coronal mass ejections (CMEs) in general, thus providing early warning of space weather.

According to the radiation theory, emissions in Hα (6563 Å) and other EUV wavelengths are intrinsically excited, reflecting the same physical condition from different aspects. The Hα observation of the Sun has a long history and are routinely taken for decades. Recently with the development of computer science including advanced hardwares and algorithms,"Deep Learning" rises and achieves remarkable success in many fields such as computer graphics and language translations, which inspires us to find the mappings between Hα images and

AIA images by deep learning. If the mappings between Hα images and AIA images in each passband are found by deep learning, the historical Hα observations can be extended to the UV and EUV passbands.

Training the deep neural networks (DNNs; Lecun et al. 2015) is a popular method for realizing artificial intelligence, which further leads to the concept of deep learning. The convolutional neural networks (CNNs; Lecun et al. 1998) are popular deep neural networks especially for image processing and computer vision. CNNs are commonly used to solve a wide variety of image prediction problems and map between two kinds of different images (Galvez et al. 2019). Usually, researchers have to provide a loss function to tell the CNNs how to minimize the differences between the output images and the target images. But sometimes it is difficult to define a loss function which is effective in a specific situation. Fortunately, Goodfellow et al. (2014) proposed Generative Adversarial Networks (GANs) which are designed to learn a loss function from the data. The conditional Generative Adversarial Networks (cGANs) are the combination of GANs and CNNs. Containing input limit conditions, cGANs are more geared to images to images mappings (e.g., Isola et al. 2016; Wang et al. 2018).

Recently several investigations were carried out to explore the translations between solar images taken in different passbands by deep learning. Park et al. (2019) conducted the generation of AIA ultraviolet (UV) and EUV images from the magnetograms of SDO/Helioseismic and Magnetic Imager (HMI; Schou et al. 2012) by the cGANs. Kim et al. (2019) further tried to generate the solar farside magnetograms, taking 304 Å images observed by Solar TErrestrial RElationship Observatory (STEREO) as inputs. These studies show that the cGANs could be used to build mappings between different telescopes onboard the same or different space missions, and the generated fake solar images matching the real observation relatively well. However, the mappings of solar images form ground-based to space-based telescopes are rare (e.g., Shin et al. 2020).

In this work, we explore whether the cGANs have the capability to map from Hα images to AIA images. In Section 2, we introduce the deep neural networks used in this study. We train the networks with the data presented in Section 3. The evaluating functions for scoring the model-generated images are displayed in Section 4. We present the results in Section 5. Summary and discussions are listed in Section 6.

2 METHODS

Conditional Generative Adversarial Networks (cGAN-s) are input-data-constrained Generative Adversarial Networks (GANs), and popular methods to learn the mappings from an input dataset (A) to a target dataset (B) (the images in A and B are represented by a and b). A cGAN usually contains two parts: the generator G and the discriminator D, which are usually two convolutional neural nets. The generator G is designed to produce the fake target image b' that cannot be distinguished from the real target image b. The discriminator D is trained to detect the fake b' from the real target b. In the process of training, the counterfeiting and distinguishing abilities of the generator G and the discriminator D are improving simultaneously. In the end, the fake image b' which is hard to distinguish from the real b is obtained when the cGAN finds the relationship between the input dataset (A) and target dataset (B). Isola et al. (2016) showed that cGANs produced reasonable results on a wide variety of image-mapping problems. The cGANs applied in this paper is the "pix2pix" model which includes the generator G (a "U-Net" based architecture Ronneberger et al. 2015) and the discriminator D (a convolutional 70×70 "PatchGAN" classifier). More detailed information about the network architectures is displayed in the appendix of Isola et al. (2016).

The objective or loss function of the cGAN in this work can be expressed as:

$$G^* = arg \min_G \max_D L_{\mathrm{cGAN}}(G, D) + \lambda L_1(G), \quad (1)$$

where the generator G tries to minimize this objective while the discriminator D tries to maximize it. $L_{\mathrm{cGAN}}(G, D)$ and $L_1(G)$ work together to make the output fake b' look like the real target b and minimize the L1 distance or relative error between the fake b' and the real b.

$$\begin{aligned} L_{\mathrm{cGAN}}(G, D) &= E_{x,y\sim p_{\mathrm{data}}(x,y)}[\log D(x, y)] \\ &+ E_{x\sim p_{\mathrm{data}}(x),z\sim p_z(z)}[\log(1 - D(x, G(x, z)))], \\ L_1(G) &= E_{x,y\sim p_{\mathrm{data}}(x,y),z\sim p_z(z)}[||y - G(x, z)||]. \end{aligned} \quad (2)$$

In the aforementioned loss functions, x and y are instances of the input a and the target b, z is the noise input to the generator and the output fake b' is represented as $G(x, z)$. The probabilities calculated by the discriminator D using real pairs (a and b) and fake pairs (a and b') are $D(x, y)$ and $D(x, G(x, z))$. In order to realize the high similarity of b' and b, we mix the GAN objective with a L_1 loss. The noise z is provided in the form of dropout on several layers of our generator G. We tried different generator configurations such as 'U-net' and residual net which resulted in generated images with similar scores. The 'U-net' is chosen in the end due to its high efficiency. After several attempts, we set the learning rate as 0.0002 in the training phase during which λ is set to be 100 which serves as the proportion of L_1 loss. The generator G and the discriminator D are trained to find optimal parameters to map from dataset A to dataset B until the $L_{\rm cGAN}$ and L_1 gradually tend to convergence. During the test phase, the b' is obtained from the input a through the established mappings.

3 DATA

The Atmospheric Imaging Assembly (AIA; Lemen et al. 2012) onboard the Solar Dynamics Observatory (SDO; Pesnell et al. 2012) has been monitoring the Sun for about 10 years. It captures images (4096×4096 pixels) of the full Sun in seven EUV passbands and two UV passbands in 94, 131, 171, 193, 211, 304, 335, 1600 and 1700 Å respectively, with the spatial resolution of 0.6″ per pixel and temporal resolution of 12 s for EUV passbands and 24 s for UV passbands. A large number of simultaneous observations in UV and EUV passbands are obtained, which provides a vast treasure trove for deep learning. We obtained SDO/AIA EUV and UV images of years 2012, 2013 and 2014 with cadence of 24 hours from the Joint Science Operations Center and processed the images to level 1.5 by the SolarSoft routine “aia_prep”. All AIA images are divided by their exposure time and downsampled to the size of 1024×1024 pixels by averaging ambient 4×4 pixels. We process the data with the routines in SunPy (SunPy Community et al. 2020).

The Global Oscillation Network Group (GONG; Hill et al. 1994) includes six stations, which are the Big Bear Solar Observatory, High Altitude Observatory, Learmonth Solar Observatory, Udaipur Solar Observatory, Instituto de Astrofísica de Canarias and Cerro Tololo Interamerican Observatory. GONG has the ability of obtaining nearly continuous observations of the Sun on the ground. Full-disk Hα line-center images (2048×2048) with cadence of about 1 minute and spatial resolution of about 1″ per pixel are obtained from GONG. From the six stations, we choose Hα images consistent with the AIA images and average their neighboring 2×2 pixels to make Hα images the same size as the AIA images. In the end, 981 pairs of SDO/AIA and Hα images with the size of 1024×1024 pixels are obtained after removing the damaged observations. We leave 327-pair Hα and AIA images (in year 2012) as the test datasets and divide the images of years 2013 and 2014 into training (500 pairs) and validation (154 pairs) datasets in chronological order.

4 EVALUATION

In order to evaluate our results, we compare the model-generated images with the observed images by the average normalized absolute error (R1), normalized mean square error (R2), percentage of good pixels (PPE10: percentage of pixels with relative error less than 10 percent) and pixel-to-pixel Pearson correlation coefficient (PCC) which are the common metrics to measure the error and correlation between two images (e.g., Galvez et al. 2019 and Park et al. 2019).

$$\mathrm{R1}_i = \sum \mid \chi_j^r - \chi_j^f \mid / \sum \chi_j^r, \tag{3}$$

where i is the serial number of evaluation samples, χ_j^r is the pixel value of the real observation images (b) and χ_j^f is that for model-generated images (b').

$$\begin{aligned} \mathrm{R2}_i &= \sum \left(\chi_j^r - \chi_j^f\right)^2 / \sum \left(\chi_j^r\right)^2, \\ \mathrm{PPE10}_i &= \frac{N\mathrm{pix}_{|\chi_j^r - \chi_j^f|/\chi_j^r < 10\%}}{N\mathrm{pix}_{\mathrm{all}}}, \end{aligned} \tag{4}$$

where $N\mathrm{pix}_{|\chi_j^r - \chi_j^f|/\chi_j^r < 10\%}$ means the number of pixels where $\frac{|\chi_j^r - \chi_j^f|}{\chi_j^r}$ is lower than 10% and $N\mathrm{pix}_{\mathrm{all}}$ is the total number of pixels in one image.

$$\mathrm{PCC}_i = \frac{\sum \left(\chi_j^r - m_{\chi^r}\right)\left(\chi_j^f - m_{\chi^f}\right)}{\sqrt{\sum \left(\chi_j^r - m_{\chi^r}\right)^2 \sum \left(\chi_j^f - m_{\chi^f}\right)^2}}, \tag{5}$$

where m_{χ^r} and m_{χ^f} are the mean of the χ_j^r and χ_j^f, respectively. We also calculate the standard deviation of R1, R2, PPE10 and PCC to evaluate the reliability and stability of the trained cGAN models. The equation is $p_{\rm std} = \sqrt{\sum_{i=1}^{n}\left(p_i - m_p\right)^2 / n}$, where m_p is the mean of the scores.

5 RESULTS

The eight mappings from Hα images to AIA images are established by cGANs, which are displayed in Figure 1. Five-hundred pairs of Hα and AIA images are collected to train the cGANs. In order to improve the universality of our trained models with limited images, we randomly cut the images (1024×1024) into 512×512 subsets and then feed the cGANs with the subsets. We train the cGANs with 200 epochs which are 100 000 iterations in total. During one iteration one pair of randomly cut subsets is fed to the cGANs and all of the 500-pair subsets are thrown into the networks in one epoch. We save the generator G and the discriminator D every 10 epochs, as a result 160 models (20 models for every eight mappings of Hα and AIA images) are collected. In the validation phase, we try to find the best trained models which get the highest scores of R1, R2, PPE10 and PCC on validation datasets (154-pair images), and then the eight best models are tested on test datasets (327-pair images). We show the R1, R2, PPE10 and PCC scores of the eight best models in the end.

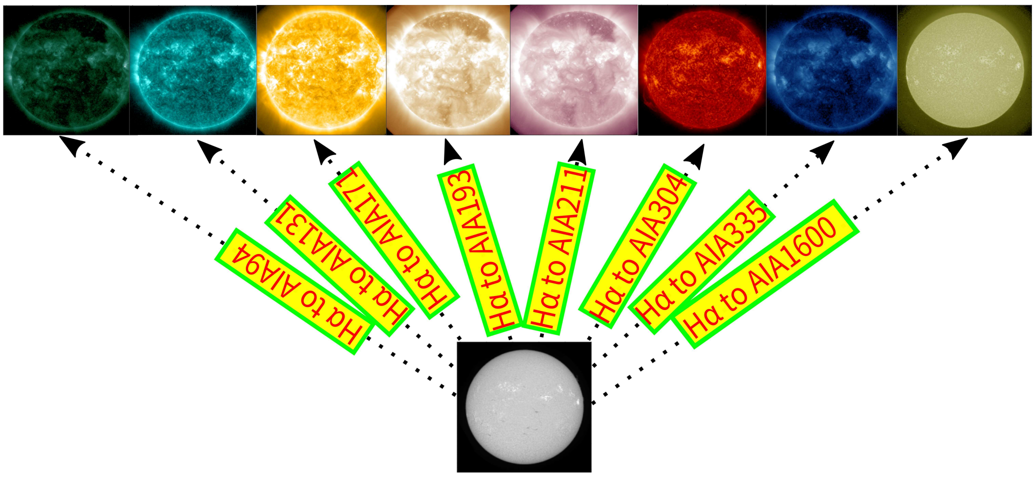

Fig. 1 This figure shows the mappings from ground-based Hα images to SDO/AIA UV and EUV images of the Sun. Eight cGAN models are trained by 500-pair Hα and AIA images which are paired images of [Hα, AIA94], [Hα, AIA131], [Hα, AIA171], [Hα, AIA193], [Hα, AIA211], [Hα, AIA304], [Hα, AIA335] and [Hα, AIA1600].

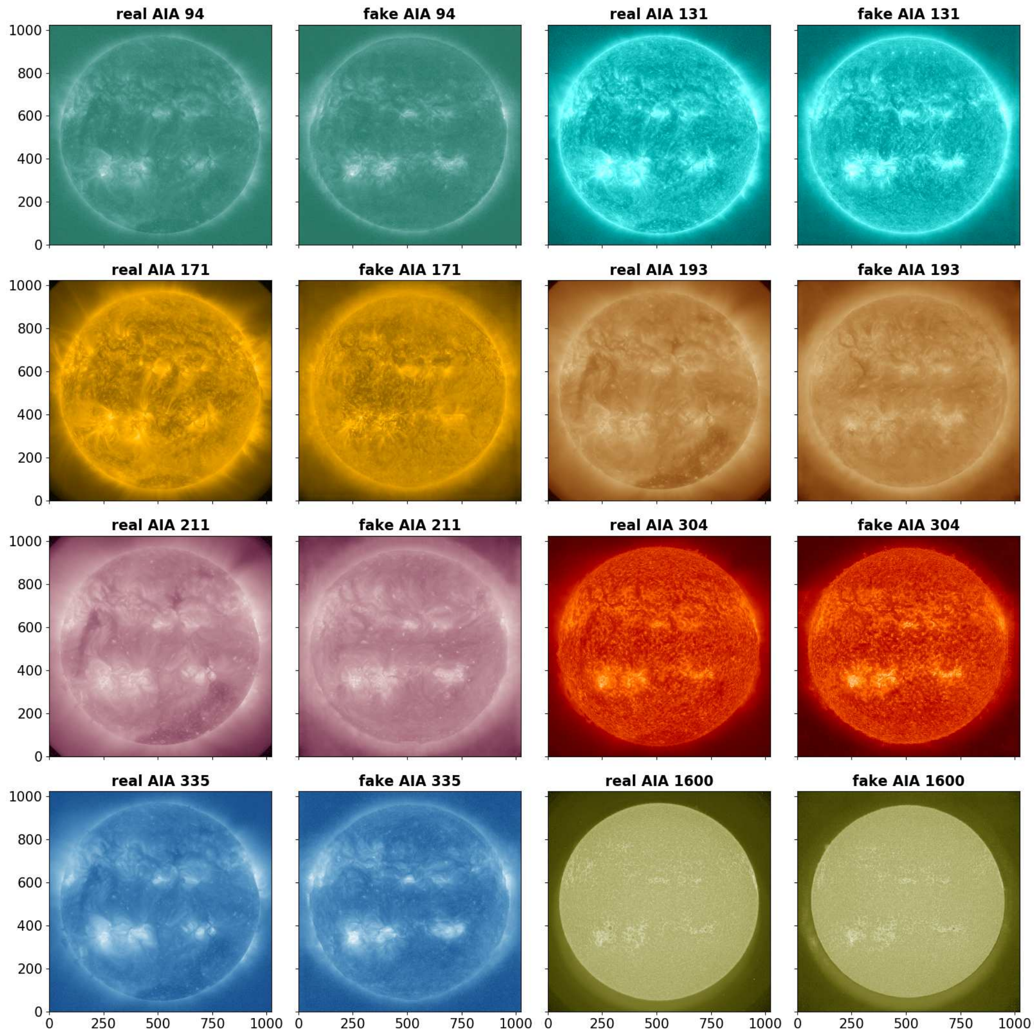

Fig. 2 Eight pairs of real and model generated images (the first of the 327 test datasets: real and fake AIA94, AIA131, AIA171, AIA193, AIA211, AIA304, AIA335 and AIA1600) are displayed in this figure. An animation of all 327 test datasets is available online at *http://www.raa-journal.org/docs/Supp/ms4798fig2movie.mp4*.

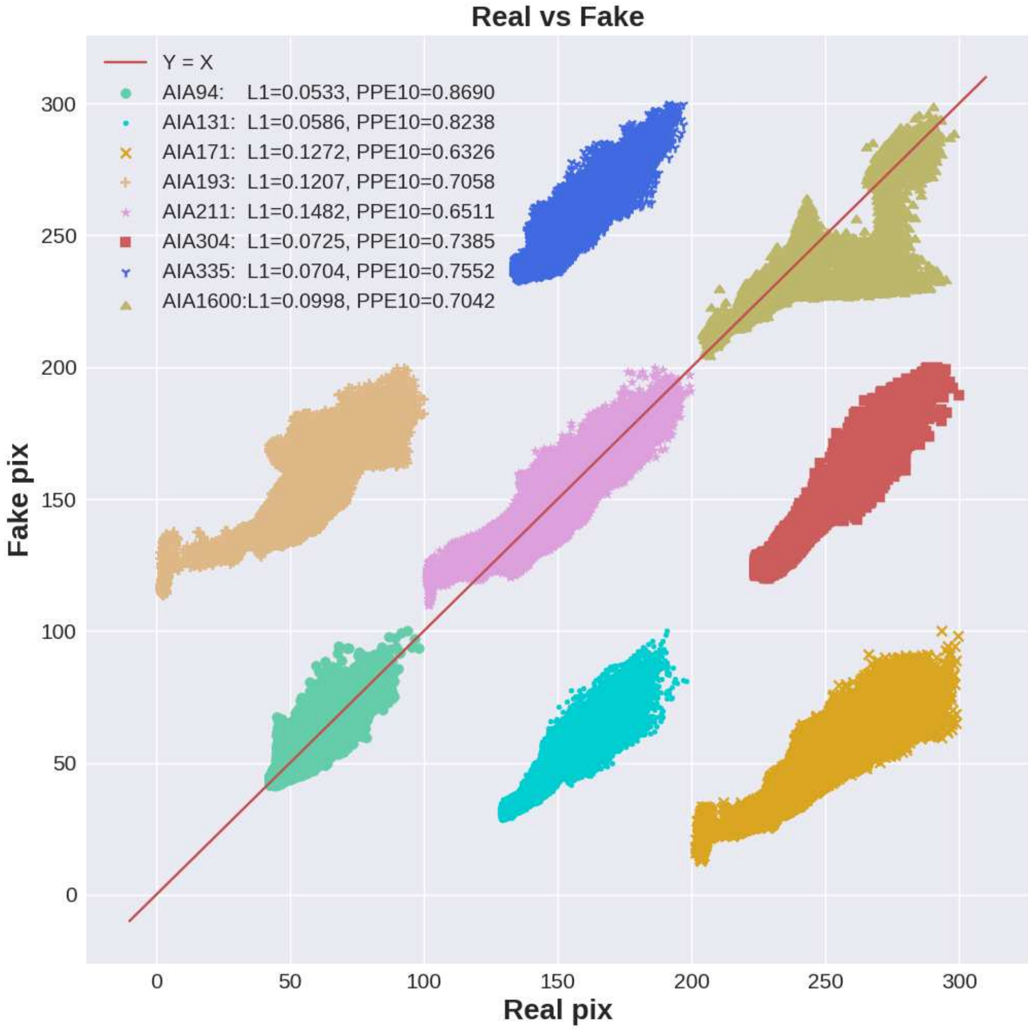

Fig. 3 The pixel values of eight pairs of real and fake images (in Fig. 2) are scattered along horizontal and vertical axes in this figure after 4×4 pixels rebinned. We renormalize the pixel values to [0:100] and parallel move the eight pairs images to the corresponding locations. The corresponding R1 and PPE10 are listed in the top left corner. An animation of all 327 test datasets is available online at `http://www.raa-journal.org/docs/Supp/ms4798fig3movie.mp4`.

Figure 2 shows the comparisons of eight pairs of real and fake AIA images. We find that the cGANs have the ability to generate AIA-like images with the large-scale structures such as large active regions and prominences matching that of the real observations. But the model generated small-scale flare loops and filament threads deviate from those in the real images. We failed to reconstruct the solar limb structures such as coronal cavities and streamers, because the Hα images possess few features of the solar limb structures.

In order to compare the results, we resize the real and fake images (1024×1024) to 256×256 images, normalize the pixel values to [0:100] and then scatter them along horizontal and vertical axes, which is displayed in Figure 3. All of the points should be located along the 45-degree line, if the fake and real images are exactly the same. We find that most of the scatter plots are shuttle shapes with narrow ends and a wide middle, which indicates that the generations of high-value pixels are better than that of the low-value pixels. The upward bending at the low-value part in the scatter plots of AIA 171, 193 and 211 Å suggests that the trained cGANs models tend to overestimate the pixel values in the solar limb regions. The listed L1 and PPE10 in Figure 3 show that the generated AIA 94, 131, 335, 304 and 1600 Å images obtain higher scores than the generated AIA 171, 193 and 211 Å images.

The mean and standard deviation of R1, R2, PPE10 and PCC on the test (327-pair images) and validation (154-pair images) datasets are displayed in Figures 4 and 5. Equations of R1, R2, PPE10 and PCC are presented in Section 4 and all of the calculations are based on image arrays after 4×4 binning. The evaluation results about the validation and test datasets are highly consistent with each other, which indicates that our trained cGANs are universal

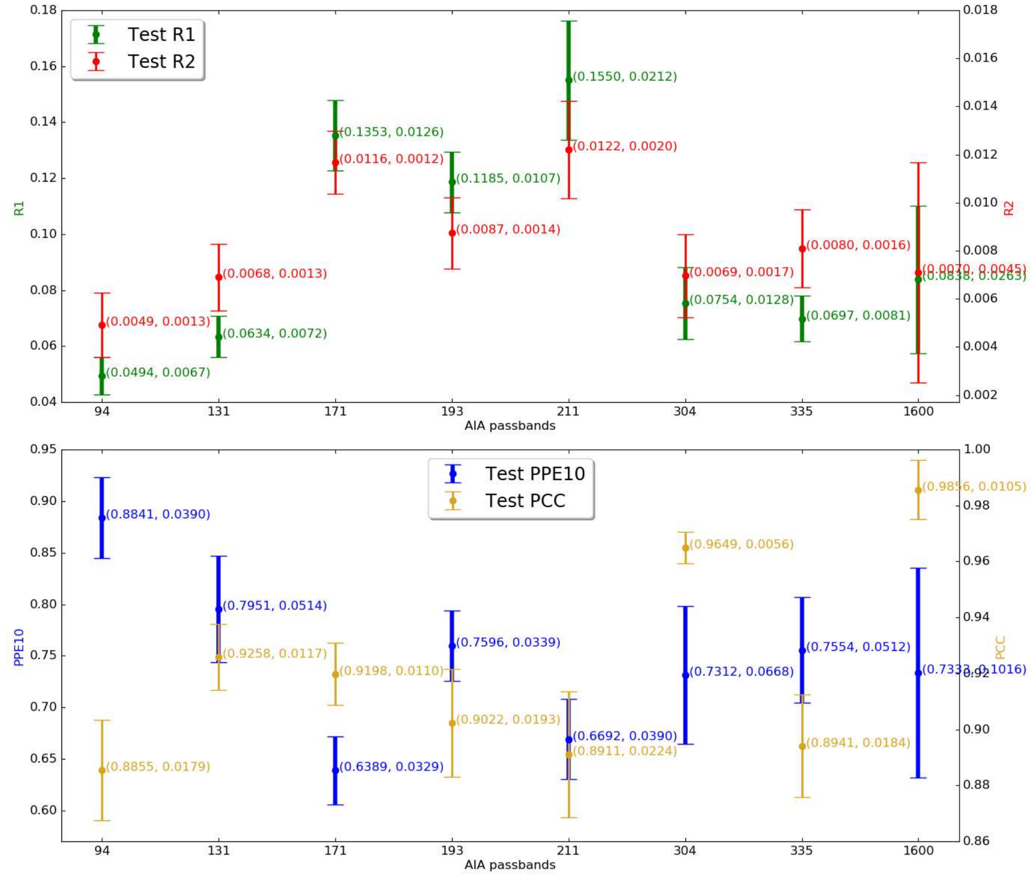

Fig. 4 The mean and Standard Deviation (SD) of R1, R2, PPE10 and PCC scores on the test datasets (327 images). The scores of the eight mappings (Hα-to-AIA) are marked by bars.

models for different datasets. Considering R1 scores, we find that the model generated AIA 94 Å images are the best with the mean and standard deviation equal to 0.0494 and 0.0067 and the generated AIA 211 Å images are worst with the mean and standard deviation being 0.1550 and 0.0212 for the test datasets. The R2 scores of the test datasets also indicate that the fake AIA 94 Å images get the highest scores (the mean and standard deviation are 0.0049 and 0.0013) and the lowest scores are obtained by the fake AIA 211 Å images (the mean and standard deviation are 0.0122 and 0.0020). The PPE10 scores in the test datasets show that the trained cGANs model of mapping from Hα images to AIA 94 Å images works best again with the mean and standard deviation of 0.8841 and 0.0390. The PPE10 of the 327 faked AIA 171 Å images is the lowest ($\mathrm{PPE10_{mean}} = 0.6389; \mathrm{PPE10_{standard\ deviation}} = 0.0329$). The mean and standard deviation of PCC for the 327 faked AIA 94 Å images are 0.8855 and 0.0179 which are the worst scores. The PCC scores suggest that the generated AIA 1600 and 304 Å images are the top two whose mean and standard deviation are 0.9856, 0.0105 and 0.9649, 0.0056 respectively. In addition to scores, the model generated AIA 1600 and 304 Å images match the corresponding real observations best according to the visual comparison as shown in Figure 2. We think that the higher similarity between the fake AIA 304 Å, 1600 Å and target real AIA 304 Å, 1600 Å images is due to the initial higher similarity of the real AIA 304 and 1600 images with the input Hα images.

6 SUMMARY AND DISCUSSION

In this work, we train cGAN models to find the mappings from Hα images to AIA94, AIA131, AIA171, AIA193, AIA211, AIA304, AIA335 and AIA1600 images. With the trained models and real Hα images, we generate the corresponding fake AIA images whose macro structures are consistent with those of real AIA images. But fine structures such as the flare loops and filament threads in the generated AIA images do not match well with the corresponding detailed structures in the real AIA images. On the one hand, we think that the information of fine structures in the Hα images is not enough to generate corresponding fine structures in the AIA images. The structures of the non-potential flare loops and filament threads observed by the AIA UV and EUV images depend on coronal magnetic fields which can be extrapolated from

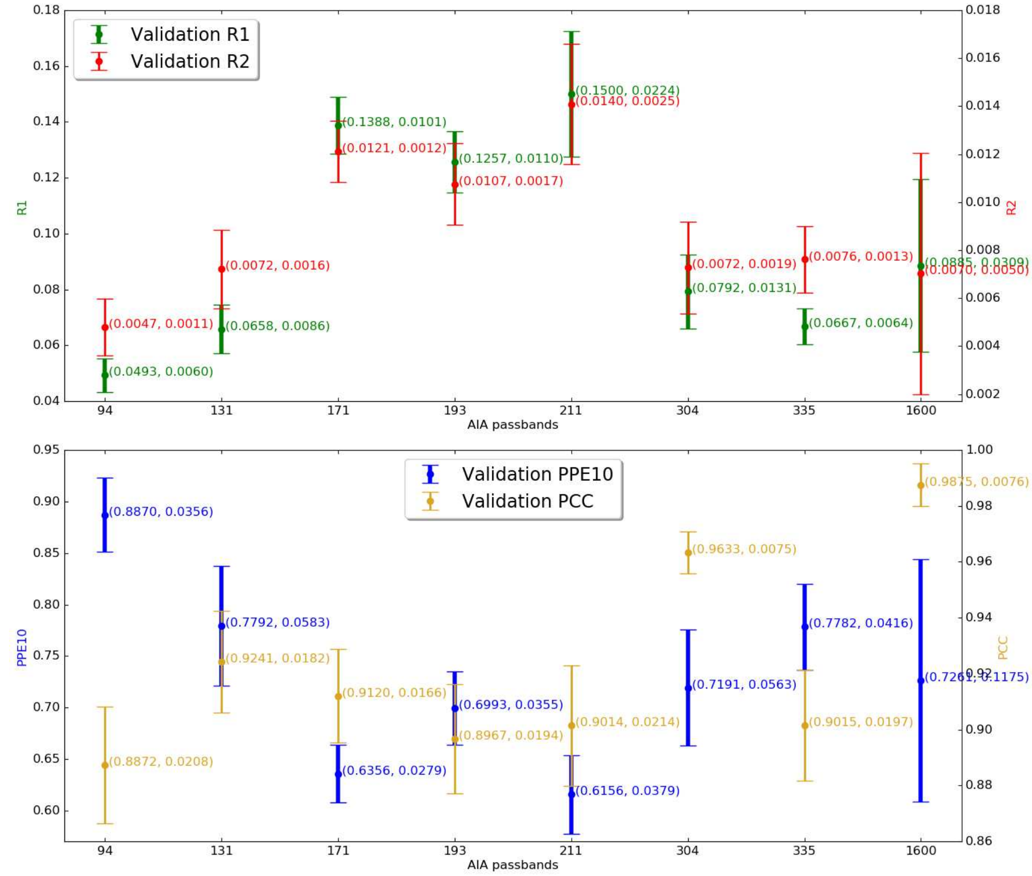

Fig. 5 Same with Fig. 4, but for validation datasets.

the photospheric vector magnetic field under the force-free-field hypothesis (e.g., Wiegelmann 2008; Guo et al. 2017). It is obvious that not only the radiation intensity but also the radiation polarization are necessary to measure the photospheric vector magnetic fields. So the information of radiation intensity (Hα images) itself is not enough to generate non-potential structures observed by AIA images. One the other hand, the GANs and cGANs are designed to solve image-to-image translations which are not one-to-one mappings. Given an input image, many output images are permissible as long as they look like the real target images. But one Hα image should have one and only one corresponding AIA image, because the observations of Hα and AIA are unique and corresponding one by one.

After synthesizing the above two aspects, we think that the cGANs are unlikely to have the ability to learn a perfect mapping between two kinds of scientific images such as Hα images and AIA images. The perfect mapping means that the mapping-generated images are consistent with the corresponding target images not only on macro structures but also on fine structures. In other words the cGANs model generated images cannot be exactly the same with the corresponding observed images. Nevertheless, cGANs do have potential development for the mappings between large amount of different solar images. We train the cGANs with datasets containing hundreds of paired scientific images. This benefits from the generator G in the cGANs being a “U-Net” based architecture which is designed to work with very few training images and yield more precise segmentations (Ronneberger et al. 2015).

There is no doubt that cGANs are good methods for image-to-image mappings and inspire us to explore the possibility of obtaining SDO/AIA Solar UV and EUV images from ground-based Hα observations. The cGANs model generated images are inaccurate and cannot replace real observations at this stage. In order to obtain much better cGANs model-generated AIA images, two ways are possible to improve the mapping results. One is that both the radiation intensity and the radiation polarization are included to train the cGANs models. The other is that considering the temporal evolution of solar observations and further constrain the cGANs. Besides, with the development and promotion of the Hα telescopes, the future Hα images with higher spatial and temporal resolutions will be applied to obtain the corresponding UV and EUV images with higher spatial and temporal resolutions, which shows a good prospect for application. Future missions such as the Advanced Space-based Solar

Observatory (Gan et al. 2019; Huang et al. 2019) and Chinese Hα Solar Explorer (Li et al. 2019) will provide data for potential applications in deep learning.

Acknowledgements We thank the community that develops the 'pix2pix' module on Github. We appreciate the team members of the SDO mission for contributing to the high-quality AIA observations. We thank the SunPy team for providing useful routines. This work utilizes data from the National Solar Observatory Integrated Synoptic Program, which is operated by the Association of Universities for Research in Astronomy, under a cooperative agreement with the National Science Foundation and with additional financial support from the National Oceanic and Atmospheric Administration, the National Aeronautics and Space Administration, and the United States Air Force. The GONG network of instruments is hosted by the Big Bear Solar Observatory, High Altitude Observatory, Learmonth Solar Observatory, Udaipur Solar Observatory, Instituto de Astrofísica de Canarias, and Cerro Tololo Interamerican Observatory. This work is supported by the National Natural Science Foundation of China (Grant Nos. 41761134088, 11790302 (11790300), 11473071 and U1731241) as well as the Strategic Priority Research Program on Space Science, CAS (Grant Nos. XDA15052200 and XDA15320301). Liming Xu is supported by Scientific Research Project of '333 Project' of Jiangsu (BRA2019310).

References

Cao, W., Gorceix, N., Coulter, R., et al. 2010, Astronomische Nachrichten, 331, 636

Galvez, R., Fouhey, D. F., Jin, M., et al. 2019, ApJS, 242, 7

Gan, W.-Q., Zhu, C., Deng, Y.-Y., et al. 2019, RAA (Research in Astronomy and Astrophysics), 19, 156

Goodfellow, I. J., Pouget-Abadie, J., Mirza, M., et al. 2014, arXiv:1406.2661

Guo, Y., Cheng, X., & Ding, M. 2017, Science China Earth Sciences, 60, 1408

Hill, F., Fischer, G., Grier, J., et al. 1994, Sol. Phys., 152, 321

Huang, Y., Li, H., Gan, W.-Q., et al. 2019, RAA (Research in Astronomy and Astrophysics), 19, 164

Isola, P., Zhu, J.-Y., Zhou, T., & Efros, A. A. 2016, in IEEE Conference on Computer Vision and Pattern Recognition, Image-to-Image Translation with Conditional Adversarial Networks, arXiv:1611.07004

Kim, T., Park, E., Lee, H., et al. 2019, Nature Astronomy, 3, 397

Kosugi, T., Matsuzaki, K., Sakao, T., et al. 2007, Sol. Phys., 243, 3

Lecun, Y., Bengio, Y., & Hinton, G. 2015, Nature, 521, 436

Lecun, Y., Bottou, L., Bengio, Y., & Haffner, P. 1998, Proceedings of the IEEE, 86, 2278

Lemen, J. R., Title, A. M., Akin, D. J., et al. 2012, Sol. Phys., 275, 17

Li, C., Fang, C., Li, Z., et al. 2019, RAA (Research in Astronomy and Astrophysics), 19, 165

Liu, Z., Xu, J., Gu, B.-Z., et al. 2014, RAA (Research in Astronomy and Astrophysics), 14, 705

Park, E., Moon, Y.-J., Lee, J.-Y., et al. 2019, ApJL, 884, L23

Pesnell, W. D., Thompson, B. J., & Chamberlin, P. C. 2012, Sol. Phys., 275, 3

Ronneberger, O., Fischer, P., & Brox, T. 2015, in Medical Image Computing and Computer-Assisted Intervention – MICCAI 2015, eds. N. Navab, J. Hornegger, W. M. Wells, & A. F. Frangi (Cham: Springer International Publishing), 234

Schou, J., Scherrer, P. H., Bush, R. I., et al. 2012, Sol. Phys., 275, 229

Shin, G., Moon, Y.-J., Park, E., et al. 2020, ApJL, 895, L16

SunPy Community, Barnes, W. T., Bobra, M. G., et al. 2020, ApJ, 890, 68

Wang, T.-C., Liu, M.-Y., Zhu, J.-Y., et al. 2018, in Proceedings of the IEEE Conference on Computer Vision and Pattern Recognition

Wiegelmann, T. 2008, Journal of Geophysical Research (Space Physics), 113, A03S02